Investigation of the ion dynamics in a multispecies plasma under pulsed magnetic fields

R. Arad,[a] K. Tsigutkin, and Y. Maron
Faculty of Physics, Weizmann Institute of Science, 76100 Rehovot, Israel

A. Fruchtman
Holon Academic Institute of Technology, Holon 58102, Israel

(Received 13 January 2004; accepted 7 June 2004; published online 26 August 2004)

The interaction between a moving magnetic-field front and a low-collisionality plasma consisting of different ion species is investigated using spatially and temporally resolved spectroscopic techniques. The experiment is carried out in a plasma-opening-switch configuration, in which a current rising to 150 kA in 400 ns is conducted through a plasma that prefills the region between two planar electrodes. Ion-species separation is found to occur, similarly to the results reported for a 80 ns duration plasma-opening-switch experiment of cylindrical geometry, which was not necessarily expected since in the present experiment plasma pushing is more substantial. The separation, in which the light-ion plasma (protons) is reflected while the heavy-ion plasma (carbon) is penetrated by the propagating magnetic-field, is investigated by determining the electron density from the temporal evolution of spectral lines, the nonprotonic ion velocities from line-emission Doppler shifts, and the proton velocity distribution from Doppler shifts of line emissions from hydrogen atoms produced by proton charge exchange. The ion dynamics is shown to be consistent with the acceleration expected from the one-dimensional Hall electric field, based on the previously published magnetic-field and electron density evolutions. Significant acceleration of the nonprotonic ions behind the magnetic-field front is observed. It is found that a significant fraction of the protons acquire a velocity that is more than twice the velocity of the magnetic piston. This phenomenon is shown to result from the time dependence of the accelerating electric field and the broad acceleration region. The lateral motion of the nonprotonic ions is also discussed. © *2004 American Institute of Physics*. [DOI: 10.1063/1.1782193]

I. INTRODUCTION

The interaction between plasmas and time varying magnetic fields is a broad topic with implications to many laboratory and astrophysical plasmas. In pulsed current-carrying plasmas the competition between plasma pushing by the magnetic-field pressure and field penetration into the plasma, together with the influence of two-dimensional (2D) and 3D effects, makes this problem very complex. Different aspects of the interaction have been investigated in numerous configurations such as theta pinches,[1] ion diodes,[2] plasma switches,[3] and plasma-beam transport across magnetic-fields.[4] In astrophysics, such problems are found in the interaction of the solar wind with the earth magnetic field,[5] in solar flares,[6] and in accretion of disks.[7]

If the magnetic-field evolution is dominated by rapid field penetration into the plasma, electron heating accounts for most of the dissipated magnetic-field energy. If, on the other hand, field penetration is little, the plasma is accelerated to the characteristic hydrodynamic velocity by the $\vec{j} \times \vec{B}$ force and the ion kinetic energy accounts for most of the dissipated magnetic-field energy.

The rate of magnetic-field penetration into plasmas is often determined by the rate of diffusion (including field diffusion that is enhanced by current-driven instabilities). However, it has been demonstrated theoretically[8–10] [within the context of electron magnetohydrodynamics (EMHD)] and experimentally[11,12] that the rate of field penetration into nonuniform plasmas can be determined by the Hall electric field. When the velocity of this Hall-induced magnetic-field penetration is larger than the characteristic hydrodynamic velocity, the plasma pushing remains little. At the extreme limit of no plasma motion, EMHD theory predicts that a sharp magnetic-field front propagates in the plasma at the Hall velocity[9] $v_H = cB/8\pi e n_e L$, where B is the intensity of the magnetic-field, c is the speed of light in vacuum, n_e is the electron density, and $L=[\partial \ln(n_e)/\partial \xi]^{-1}$is the characteristic scale of the electron-density variations in the direction (ξ) of the current flow. The predicted (low) ion velocities close to that limit scale linearly as a function of the ion charge-to-mass ratio, as demonstrated experimentally.[12] As expected in the case that magnetic-field penetration velocity is high, the EMHD model predicts that the electrons acquire most of the magnetic-field energy dissipated due to the field penetration.[13,14]

Cases of spatial ion separation have been addressed in various configurations.[15–18] Recently, however, a special case of ion separation, in which a light-ion plasma is pushed ahead while a heavy-ion plasma lags behind the magnetic piston, was discovered.[19,20] This first observation of simultaneous field penetration into the heavy-ion plasma and reflec-

[a]Present address: Soreq Nuclear Research Center, Yavne 81800, Israel; electronic mail: fnarad@yahoo.com

tion of the light-ion plasma was made in a relatively short-duration (~80 ns) plasma-opening-switch (POS) experiment with a plasma that is composed of more than one ion species, in which magnetic-field penetration due to the Hall field was expected to be dominant. In the presently discussed longer-time experiment, a plasma of a higher density is used, for which the effect of plasma pushing, relative to Hall penetration, is expected to be larger. Also, in the present experiment the fractional density of the heavier ions (carbon ions) is larger than in the short-duration experiment, which together with the longer time scale causes a larger effect of the heavier-ion dynamics on the electron-density evolution in the plasma. However, the phenomenon of simultaneous reflection and penetration was found also in the present configuration,[21] similar to the short-time experiment. The independence of the magnetic-field evolution on the relative direction of the current flow and the plasma density gradient[21,22] contradicts the predictions of the simple Hall-field theory, suggesting that a more complex scenario is responsible for the rapid magnetic-field penetration into the heavier ion plasma.

Our experiments are carried out in a configuration commonly known as a POS,[3,23] in which a prefilled plasma conducts a current between two electrodes. The present paper focuses on the measurement of the ion dynamics during the interaction with the propagating magnetic-field piston. Diagnostic techniques based on Thompson scattering[24] are impractical for the relatively low electron density and high temporal resolution required. Also, laser-induced fluorescence[25] may yield only a limited advantage (over emission spectroscopy) due to the high electron energy that continuously populates the excited levels that may be pumped by such a scheme. Ion-velocity studies using emission spectroscopy (using Doppler shifts) suffer from a serious drawback, namely, integration along the line of sight. Hence, in past studies of POSs, one preferred indirect method for inferring the ion motion, based on interferomentric measurements[26] of the electron density. Such interferometric measurements have been performed along chordal[27] and axial[28] lines of sight in coaxial configurations and along the θ-like direction in a planar configuration.[29] These measurements showed a drop in the electron density, which could be associated with a drop in the ion density. However, the spatial integration along the line of sight did not allow for tracking the correlation between the electron density drop and the evolution of the magnetic field, obtained from magnetic-probe measurements.[27,29,30] Also, evidently, observations of variations in the electron density do not allow for discerning the motion of different ions in the plasma.

An alternative route implemented plasma doping techniques together with emission spectroscopy to obtain spatially resolved velocity measurements of different nonprotonic ionic species in the plasma using Doppler shifts of emission lines.[12] Also in these studies, the time-dependent electron density was measured using the intensity of low-lying levels,[19] and the magnetic-field distribution was obtained from Zeeman splitting.[11] However, in those experiments the limited knowledge on the plasma composition and the lack of knowledge of the proton velocities did not allow for discerning the relatively complex ion dynamics to be described below.

In the present experiments, the plasma doping techniques[31,32] were improved to allow for doping gaseous as well as solid elements, and, combined with the planar geometry, yielded higher spatial resolution in the magnetic-field-propagation direction. This improvement in resolution, together with the knowledge of the previously obtained plasma composition,[32] allows for a detailed comparison of the ion dynamics and the accelerating magnetic field. The complication brought about by the ionization during the acceleration, which causes a difficulty in comparing the observed velocities with the accelerating magnetic-field gradient, is overcome by using various dopant species for the measurements as will be shown below.

Here, a technique for measuring the proton velocities, employing charge-exchange spectroscopy, allowed for by using hydrogen dopant with which the accelerated protons undergo charge exchange, was developed.[21] The proton velocity distribution is thus obtained from the shifted H_α profile, while the velocity distributions of the nonprotonic ions are obtained from Dopper-dominated spectral line profiles of different ions.

The ion-velocity measurements are augmented by measurements of the time-dependent electron density, which, together with the measured magnetic-field distribution, yield the accelerating electric field as a function of space and time. The observed ion velocities are compared to the expected acceleration based on the obtained electric field, showing good agreement. The measured local electron density evolution and the axial motion of the protons and the nonprotonic ions allow for inferring the extent of the lateral motion of the nonprotonic ions.

Our measurements also allow for analyzing the ion acceleration and enable us to elucidate the momentum imparted to each of the plasma constituents. The momentum partitioning between the light and heavy ions is found to agree with the predictions of a previously presented time-independent model of ion species separation by a magnetic piston.[20] In a subsequent publication[33] that reports on the electron heating and the non-Maxwellian electron energy distribution, these data will be employed to explore the energy dissipation mechanism, associated with the magnetic-field penetration into the plasma.[12,34]

II. EXPERIMENTAL ARRANGEMENT

The experimental system consists of two planar, 14 cm wide, electrodes separated by a 2.5 cm gap, as shown in Fig. 1. In the 9 cm long plasma prefilled region, the electrodes consist of eight 1 mm diameter wires with a geometric transparency of 93%, allowing for unimpeded plasma flow into the anode-cathode (*A-K*) gap and minimizing the effects of plasma stagnation. The load for the current downstream of the plasma is a short circuit with a 30 nH inductance. A current that rises to 150 kA in ≈400 ns generates a magnetic field of ~10 kG between the two electrodes. The following coordinates are defined: $x=0$ is the cathode surface, $y=0$ is the center of the electrodes, and $z=0$ is the generator side

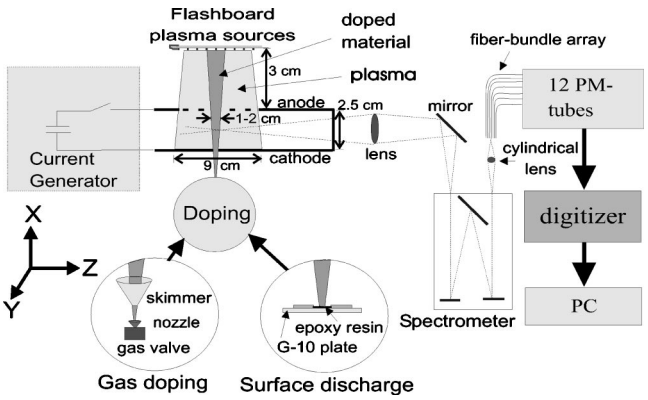

FIG. 1. The experimental system. The interelectrode region is prefilled with plasma from two flashboard plasma sources. Two techniques are used to locally dope the plasma with various elements. Light is collected from the doped column into the spectrometer. A cylindrical lens focuses the output of the spectrometer onto a fiber-bundle array that transmits the light to 12 photomultiplier tubes.

edge of the transparent anode (note that the magnetic-field propagation direction is denoted by z, in analogy to coaxial plasma switches).

Two flashboard-plasma sources,[32,35] driven by a single 2.8 μF capacitor charged to 35 kV, are mounted 3 cm above the anode wires and are operated 1.1 ± 0.05 μs prior to the main current pulse. Each flashboard consists of eight chains with the current through each chain reaching a peak value of 6.5 kA at $t=1.2$ μs. The electron density is found to vary from 3×10^{14} cm^{-3} near the cathode to 7×10^{14} cm^{-3} near the anode and the electron temperature prior to the application of the current pulse is found to be 6.5 ± 1 eV. In the middle of the A-K gap the plasma consists of protons ($n_{\text{protons}}=2\pm1\times10^{14}$cm^3), carbon ions ($n_{\text{carbon}}=1.0\pm0.4\times10^{14}$ cm^{-3}, mainly C IV with smaller densities of C III and C V), and O IV ($n_{\text{O IV}}=1\pm0.5\times10^{13}$cm^{-3}). In the analysis that follows the O IV will be considered as a part of the "carbon plasma" since it has similar charge-to-mass ratio and demonstrates similar dynamics. The total density of heavier impurities such as Ni, Fe, Cu, and Si is found to be $<1\times10^{13}$ cm^{-3}. A detailed investigation of the prefilled plasma parameters can be found in Ref. 32.

In order to perform spatially resolved spectroscopic measurements the plasma is doped with various elements using two doping techniques. The gas doping arrangement,[31] consisting of a fast gas valve, a nozzle, and a skimmer, is mounted below the cathode. The gas density can be varied from 10^{13} to 10^{15} cm^{-3} and the FWHM of the gas beam perpendicular to its injection direction can be varied from 1 to 2 cm.

For doping solid materials[32] we use an electrical discharge over an epoxy resin mixed with the desired element on a small board, placed 2 cm below the cathode. The discharge is driven by a 2 μF capacitor charged to 6 kV. For the short-time delays used in the present experiments, the electron density in the plasma produced by the surface-flashover doping discharge was found to be less than 1×10^{13} cm^{-3} (determined spectroscopically), ensuring no significant effect on the flashboard-plasma parameters. The spatial resolution along the line of sight obtained using this doping technique is 1.5–3 cm, depending on the x position.

The uv visible spectroscopic diagnostic system (also shown in Fig. 1) consists of a 1 m spectrometer equipped with a 2400 grooves/mm grating. The light from the doped column is collected in the y or z directions and is imaged onto the spectrometer. A cylindrical lens images the light at the output of the spectrometer onto a rectangular fiber-bundle array allowing for observations with different spectral dispersions in the range of 1 Å/fiber to 0.07 Å/fiber, where the instrumental spectral resolution for a typical slit width of 30 μm is 0.06 Å. The dispersion and resolution were measured with a 3% accuracy. The optical-fiber array consists of 12 fiber bundles that transmit the light into 12 photomultipliers with a 7 ns temporal resolution. The spatial resolution along the line of sight, determined by the doped-column width, is 1–3 cm, whereas the resolutions in the orthogonal directions, determined by the spectrometer input slit and the imaging optics, are 0.1 cm in the x direction and 0.4–1 cm in the y or z directions, depending on the direction of observation. The optical system is absolutely calibrated with an accuracy of ±30%.

III. RESULTS

A. Data analysis

All spectral lines observed in this study are optically thin, allowing for a direct determination of the respective absolute upper-level populations. To analyze the spectral profiles we fit Gaussians for each of the line components whose width is analyzed assuming instrumental and Doppler broadenings (Stark broadening and Zeeman splitting are small in the present measurements, except for the He I 6678 Å line that is dominated by Zeeman splitting and used for measuring the magnetic field). The ion-velocity distributions are obtained from line profiles dominated by Doppler broadening. The measured line intensities are analyzed with the aid of a time-dependent collisional-radiative (CR) code,[32,36] to which the initial plasma composition, the time-dependent electron energy distribution,[33] and electron density are inputted as parameters. The calculated time-dependent level populations are then compared with the measured line intensities.

B. Magnetic-field propagation

The magnetic field was studied from Zeeman splitting of doped He I, as reported previously,[22,37] and the magnetic-field front was found to propagate axially at a constant velocity. The evolution of the magnetic-field profile is affected by the time dependence of the generator current and by the axial propagation of the magnetic field. Thus, we fit the observed magnetic-field distribution by the expression

$$B(z,t) = B_0\frac{t}{\tau}[1-(z-z_0)/v_{\text{B}}t]^p, \tag{1}$$

where v_{B} is the magnetic-field propagation velocity and $z_o=-2.2$ cm is the position of the vacuum-plasma boundary at the generator side (assumed to be constant in time). The

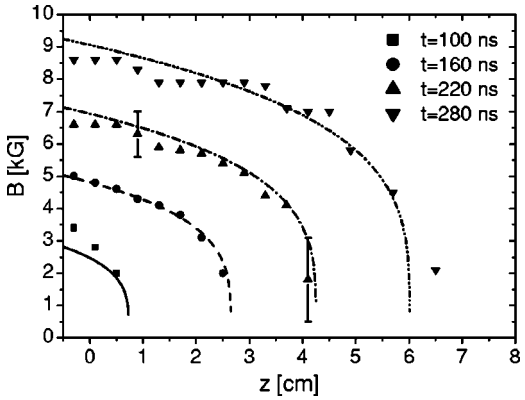

FIG. 2. The magnetic-field distribution as a function of z at 1 cm from the cathode surface in the middle of the electrode y dimension. The spatial resolution is ±0.1, ±1, and ±0.2 cm in the x, y, and z directions, respectively. The measurement error is ±1.2 kG for $B<4$ kG and ±0.7 kG for $B>5$ kG. The experimental points are fitted by Eq. (1).

amplitude of the generator-side magnetic field is obtained from the measured upstream current and is found to be $B_0=10$ kG at time $\tau=300$ ns. The parameter p describes the shape of the magnetic-field profile so that when $p\rightarrow 0$ the axial profile of the magnetic field becomes rectangular while in the limit $p\rightarrow 1$ it decreases linearly with z. A best fit to the experimental data is obtained with $p=0.25$ and $v_B=3\times 10^7$ cm/s. In the different experiments in the present work v_B varied in the range $(3-3.6)\times 10^7$ cm/s. Figure 2 shows the evolution of the axial distribution of the magnetic field at $x=1$ cm for different z positions.

C. Axial ion velocities and their scaling

1. Velocities of nonprotonic ions

The local axial velocity of He II doped in the plasma is measured using the $n=4-3$ transition ($\lambda=4686$ Å). Figure 3 shows the velocity as a function of time in experiments in which the helium was injected at $z=0$, 4, and 8 cm. An average acceleration of $(9\pm 1)\times 10^{13}$ cm/s^2 is seen at $z=0$ and 4 cm, while the acceleration at $z=8$ cm is twice larger. The axial motion of He II is <1 cm during the 50–100 ns acceleration, which is less than the initial 1.2 cm doped column

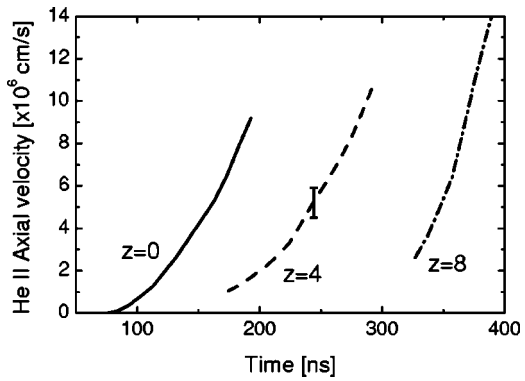

FIG. 3. Axial velocity of He II accelerated by the magnetic-field gradient, obtained from the Doppler shift of the He II 4685.5 Å line at different axial positions for 1 cm from the cathode. The velocities are only shown for the times for which the light intensity is sufficiently high.

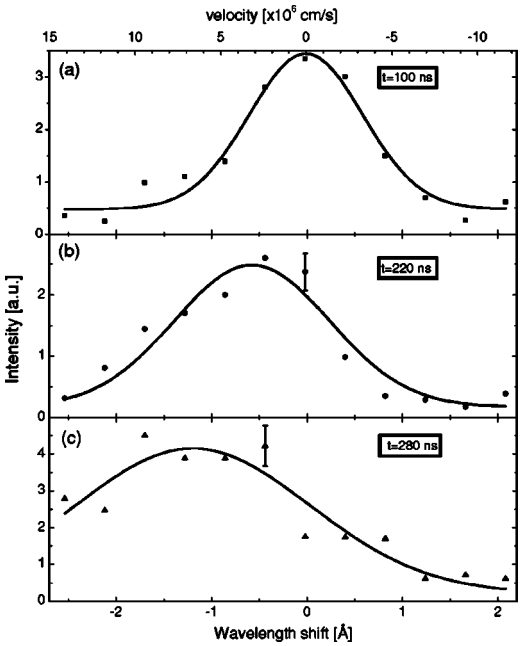

FIG. 4. Spectral profiles of the Li II $2p(^3P)$-$2s(^3S)$ transition at $t=100$, 220, and 280 ns at $x=1$, $y=0$, and $z=3.5$ cm. The top axis indicates the corresponding ion velocity, positive velocities being in the $+z$ direction. The error bars indicated are due to the signal statistical noise. The experimental points (symbols) are fitted by a Gaussian (solid line).

width. Figure 3 shows that the start of the He II acceleration propagates axially at an average velocity of $(3.3\pm 0.3)\times 10^7$ cm/s, consistent with the magnetic-field propagation velocity. Collisional-radiative calculations, based on the measured electron density and EED, show that during the acceleration a significant ionization of He I occurs, which produces He II at relatively low velocities. Thus, inferring the He II acceleration from the velocities shown in Fig. 3 yields lower-limit values. It is estimated that the peak axial He II acceleration is ~30% higher than deduced from the data presented in Fig. 3. We note that the continuous ionization of He I also tends to broaden the He II velocity distribution.

Use of dopants with a negligible ionization allows for obtaining the ion acceleration more reliably. To this end, we used the surface-flashover technique for doping lithium and boron, where the neutral-atom fractions are negligible. Figure 4 shows the Li II 5485 Å line profile at three times, obtained from axial observations for $z=3.5$ cm. The profiles demonstrate the lithium ion acceleration towards the load and the rise in the broadening of the velocity distribution. The peak mean Li II axial velocity is found to be $(7\pm 1)\times 10^6$ cm/s at $t=280$ ns, which is ≈4.5 times lower than the magnetic-field propagation velocity.

Note that such a broad ion-velocity distribution (corresponding to a kinetic energy of hundreds of eV) is unlikely to result from the low-rate ion collisionality or from ion heating due to the previously observed turbulent electric fields.[22] It is possible that it results from the formation of small-scale magnetic-field structures, which leads to ion acceleration in various directions, as suggested previously.[22]

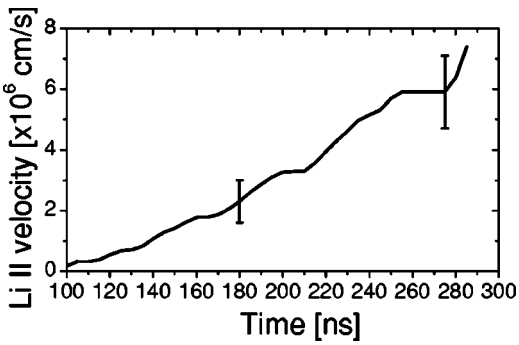

FIG. 5. Li II axial velocity as a function of time at $x=1$, $y=0$, and $z=3.5\pm1.5$ cm.

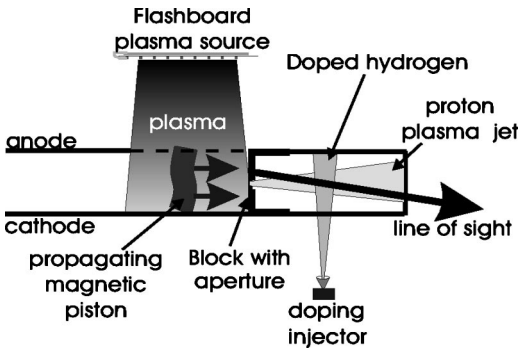

FIG. 6. The arrangement used for charge-exchange spectroscopy of the accelerated protons. Molecular hydrogen is injected about 3 cm downstream of the plasma rear edge. Light from the fast hydrogen atoms resulting from charge-exchange processes is collected at an angle of 5° with the z axis. An aperture (0.5×5 cm) at the rear edge of the plasma is used to block the light from the main plasma (measurements with no aperture yielded similar results). The velocity distribution of protons that undergo charge exchange is obtained from the H_α profile.

Figure 5 shows the mean Li II axial velocity as a function of time in the middle of the plasma. The acceleration is approximately constant and is found to be $(5.4\pm0.8)\times10^{13}$ cm/s^2. It is also evident from a comparison of Figs. 5 and 2 that the acceleration period approximately coincides with the rise of the magnetic field within the doped column.

Using similar measurements for B II it is found that the peak axial B II velocity is $(6\pm1)\times10^6$ cm/s and the mean acceleration is $(3.6\pm0.6)\times10^{13}$ cm/s^2. The axial velocity of Ar III, obtained from the 3286 Å line, showed a lower peak velocity $(7\pm2)\times10^5$ cm/s.

The axially integrated axial velocity of C III in the plasma, measured using the 2297 Å line, is found to rise to $(9\pm1)\times10^6$ cm/s at the end of the current conduction together with a rise in the line width, corresponding to a thermal velocity of $\pm(8\pm1)\times10^6$ cm/s. The effect of C II ionization during the C III acceleration is small ($<10\%$) due to the low C II density.

2. Proton velocity measurements

Knowledge of the proton velocity is essential for understanding the ion motion in the plasma because of the distinct difference between the dynamics of the protons and that of the heavier ions in the plasma. In the present work, the proton-velocity distribution was obtained from charge-exchange spectroscopy.[21]

The protons accelerated by the magnetic field undergo resonant charge exchange with a hydrogen-gas column injected downstream of the plasma, see Fig. 6. The Doppler shift of H_α of the resultant hydrogen atoms is then used to obtain the proton velocity.

The H_2 density in the 2.5 cm wide injected column is $(1.5\pm0.5)\times10^{15}$ cm^{-8}. Based on the cross section for the proton charge exchange with molecular hydrogen ($3.7\pm2\times10^{-16}$ cm^2) and with the possibly produced atomic hydrogen ($2.3\pm0.5\times10^{-15}$ cm^2) for the relevant proton energy range,[38,39] it is estimated that most of the protons undergo charge exchange in the injected hydrogen column.

Measurements are performed by scanning the blue tail of H_α in three consecutive shots so that the array of photomultipliers monitored 36 points on the wavelength scale, which yields a resolution of 3×10^6 cm/s in the velocity range from -0.5×10^7 to 9×10^7 cm/s.

The H_α profile shown in Fig. 7 demonstrates the presence of fast protons with velocities $(4-9)\times10^7$ cm/s. Since the probability for charge exchange is nearly independent of the proton velocity (for the present velocity range), the profile shown in Fig. 7 represents the proton-velocity distribution. The average proton velocity is thus seen to be $\approx7\times10^7$ cm/s, which is 2.1 ± 0.2 times the magnetic-field velocity [$(3.3\pm0.3)\times10^7$ cm/s in these measurements]. This finding is in agreement with the predictions of the specular-reflection model.[40]

As seen in Fig. 7, protons are also reflected at velocities lower and higher than twice the piston velocity. The low velocities are probably due to incomplete acceleration of part of the protons or due to partial proton pushing in the lateral directions. The mechanism of the higher velocities will be discussed in Sec. IV.

In order to verify that the proton velocity obtained above reflects the velocity distribution of most of the protons in the plasma we confirmed that the time-integrated proton flux is comparable to the initial number of protons in the prefilled plasma. To this end, we performed experiments to obtain a lower limit of the proton-plasma density using Mg II line

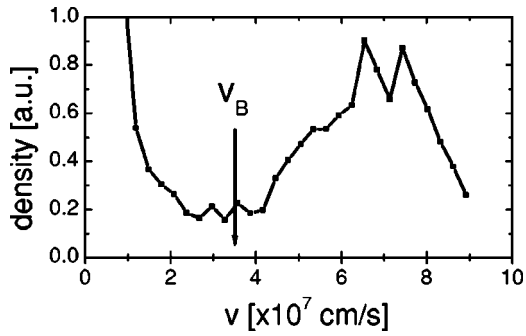

FIG. 7. The observed H_α spectral profile integrated over $t=250-300$ ns (the wavelength scale is replaced by a velocity scale). The large signal at $v<2\times10^7$ cm/s is due to the emission from the doped (slow) hydrogen atoms, while the signal for the higher velocities is due to the charge-exchange-produced hydrogen. Also marked is the magnetic-field velocity v_B.

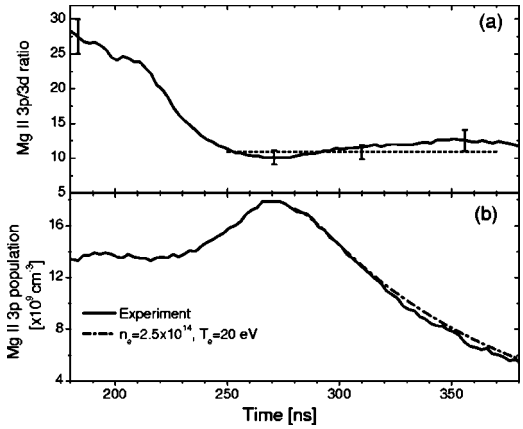

FIG. 8. (a) The measured Mg II $3p/3d$ population ratio at $x=1.2$ cm, $y=0$, and $z=9$ cm (solid line) and predictions of the collisional-radiative code. (b) The drop of the Mg II $3p$ population due to ionization (solid line) and the predictions of the CR modeling.

ratios (in a manner similar to that described in Ref. 22). In these experiments, magnesium was injected downstream (using the surface-flashover discharge instead of the hydrogen doping). The electron density and the neutral-magnesium density in the magnesium cloud were $(7\pm1)\times10^{13}$ cm^{-3} and $<10^{13}$ cm^{-3}, respectively. Determination of the electron-density rise in the magnesium cloud due to the proton-plasma propagation yields the proton-plasma density.

Figure 8(a) shows the measured time-dependent Mg II $3p/3d$ population ratio in the magnesium-dopant column. These measurements show that the ratio between the Mg II $3p$ and $3d$ populations, initially being 25–30 drops to 11 ± 1 during the flow of the proton plasma through the dopant. In order to determine n_e we use our CR calculations to fit the Mg II $2p/3d$ ratio as a function of time. However, this ratio also depends on the electron energy distribution, which is not known. In order to address this difficulty we use the observation of the B IV 2821 Å line, originating from the $2p(^3P^0)$ level that lies at about 200 eV, to show that a large fraction ($>30\%$) of the electrons have energies higher than 200 eV. This finding lowers the sensitivity of the determination of n_e to the details of the electron energy distribution at the dopant during the flow of the proton plasma. Using repeated CR calculations it is found that the uncertainty in the electron energy distribution makes the dashed line shown in Fig. 8(a) replicated by using electron densities between 2.2×10^{14} cm^{-3} and 3.6×10^{14} cm^3 (the lower electron density corresponds to the higher mean electron energy). We thus conclude that the electron density in the doped magnesium column during the encounter with the pushed proton plasma is $(2.9\pm0.65)\times10^{14}$ cm^{-3}. The proton density at this time is obtained by subtracting the initial electron density in the magnesium cloud, giving $(2.2\pm0.7)\times10^{14}$ cm^{-3}. Note that this density can only be attributed to protons, since the velocities of all other ions are too low to allow for their arrival at the measurement position.

Figure 8(b) shows that the electron density that reproduces the measured magnesium line ratio also satisfactorily explains the drop of the magnesium line intensities, which presumably result from the ionization of the doped Mg II. The ionization times suggest an electron density that is $\approx10\%$ higher than the density obtained from the line ratios.

The Stark broadening of H_α and H_β observed in the y direction was also used to determine the electron density of the proton plasma, similarly to the measurements described in Ref. 32. However, due to the possible effect of turbulent electric fields (see, for instance, Ref. 12), this technique only yields an upper limit for the electron density. These measurements yielded an electron density of $(2.6\pm0.6)\times10^{14}$ cm^{-3}, in good agreement with the magnesium data. Moreover, using our collisional-radiative calculations, we used the absolute intensity of the Doppler-shifted H_α emission to obtain the total fast-hydrogen density, expected to be equal to the proton density, since most of the protons are expected to undergo charge exchange. The proton density thus determined is found to be consistent with the value obtained above, albeit, with a larger uncertainty due to the higher sensitivity to the unknown details of the electron energy distribution.

Using the combined proton density of the magnesium and hydrogen data, $(2.4\pm0.7)\times10^{14}$ cm^{-3}, the mean proton velocity, a lower bound for the time duration of the proton-density rise (100 ns), and assuming that our measurement at $x=1$ cm represents the proton flux in the entire A-K gap, it is estimated that the total proton flux downstream of the plasma is at least a few tens of percent of the initial proton number in the plasma.

It is interesting to compare the spectroscopic observations with previously performed Faraday-cup measurements[41] in which time-of-flight data were obtained using measurements with an array of four Faraday cups ($\phi=0.025$ cm), with transverse magnetic field ($B\sim1$ kG). These measurements revealed an ion signal presumably resulting from a proton-plasma propagating axially at an average velocity of $(6.5\pm1.5)\times10^7$ cm/s, consistent with the proton velocities obtained from charge-exchange spectroscopy. The current density was found to be between 100 and 150 A/cm^2, which corresponds to an ion density of $(1-1.5)\times10^{13}$ cm^{-3}, significantly lower than the proton density obtained spectroscopically. Faraday-cup saturation or incomplete insulation of the electron current, as has recently been observed[42] in experiments in which Faraday-cup signals were compared with spectroscopic data, is believed to be the reason for the low density inferred using this method.

D. Electron density evolution

Determination of the local temporal evolution of the electron density in the plasma during the magnetic-field evolution is of high advantage, in comparison to the line-integrated charge-exchange spectroscopy that yielded the proton-plasma flow downstream of the plasma, and offer additional information on the ion dynamics.

The electron density is studied from the time-dependent B III $2p$-level population (while the electron density distribution prior to the application of the current pulse was determined from Stark broadening of hydrogen[32]). The electron density is obtained by comparing the observed evolution of the B III $2p$-level population to predictions of collisional-

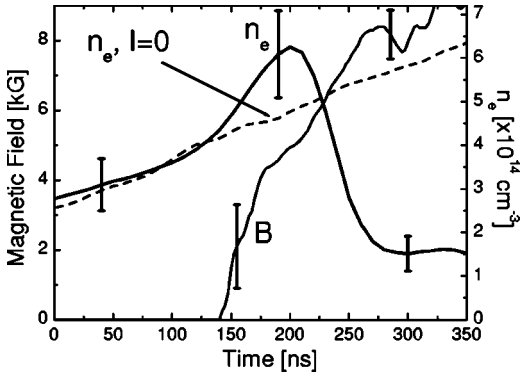

FIG. 9. The time-dependent magnetic field (averaged over two discharges) and electron density measured in separate experiments at $x=1$ and $z=3.7$ cm in the middle of the y-electrode dimension. The dashed curve shows the electron density without the application of the current pulse.

radiative calculations that account for the electron temperature variations, ionization processes, and the boron flow (the details of this analysis have been described previously[22]).

Figure 9 shows the electron density and the magnetic-field observed at the same position as a function of time. It is seen that the electron density rises with the magnetic field until the field reaches a value of ~ 5 kG, and then drops sharply as the magnetic field continues to rise. This finding is seen for all positions with the density reaching its peak value for magnetic fields of 4–5.5 kG. The drop of the electron density is found to vary across the *A-K* gap. In the middle of the gap ($x=1$ cm, see Fig. 9) the density drops to $(1.5\pm0.5)\times10^{14}$ cm^{-3} at $t=300$ ns, near the anode ($x=1.8$ cm) it only drops to $(4\pm1)\times10^{14}$ cm^{-3}, and near the cathode it drops to $(1\pm0.4)\times10^{14}$ cm^{-3}, i.e., it drops noticeably less near the anode.

As discussed previously[22] the electron density rise is due to three factors: the continuous flow of the flashboard plasma (as shown by the dashed line in Fig. 9), ionization resulting from the rise in the electron energy[33] (causing a rise in the electron density of $10\pm5\%$ at $t=200$ ns), and the proton-plasma reflection within the current channel. The lack of detailed knowledge of the proton dynamics does not allow for quantifying the rise of the electron density due to the proton-plasma reflection. Note that the velocities of the non-protonic ions are too low for times <210 ns to cause a rise in the electron density (see Fig. 3, for $z=4$ cm).

At $t>200$ ns a substantial drop in the electron density is seen (by four to five times at $x=1$ cm compared to the density without the current pulse). Based on the density of the reflected proton plasma (which is found to be consistent with the initial proton density in the plasma, see Sec. II), the electron density is estimated to drop to $(3.5\pm1)\times10^{14}$ cm^{-3} as a result of the proton reflection. This value, being twice higher than the measured electron density at $t=300$ ns, leads to the conclusion that a fraction of the carbon plasma is also pushed from the middle of the *A-K* gap.

Based on the measured carbon-ion axial velocities, we estimate their axial displacement to be ≈1 cm at $t=300$ ns, which is much smaller than the plasma length. Also, using Doppler-dominated line profiles observed in the y direction, the ion velocities in this direction were found to remain low throughout the pulse. These findings lead us to suggest that part of the carbon plasma is pushed in the x direction (towards the electrodes). Since the extent of the plasma region viewed in the x direction is ~1 cm, carbon-ion velocities in the x direction about 10^7 cm/s, i.e., comparable to the measured axial velocities, must then be assumed, in order to explain the density drop that occurs within 100 ns. We note that the density of the ions heavier than carbon in the plasma is too small[32] to be considered in this discussion.

IV. DISCUSSION

We here discuss the mechanisms that are responsible for the observed plasma dynamics and the electromagnetic evolution. As is described in detail in the following sections, for the observed magnetic field and the inferred electric-field evolutions, we are able to explain the observed dynamics of the various ion species. In Sec. IV A the ion separation is described, followed (in Sec. IV B–IV E) by a detailed calculation, incorporating the effect of the time dependence of the magnetic field, which satisfactorily explains the motions of the heavy ions and the protons.

The evolution of the magnetic field was discussed in detail in Ref. 22. We explained there that the mechanism of field penetration is still unclear, although it is expected to be related to the Hall field. The penetration seems to be too fast to be explained by the plasma initial nonuniformities. Furthermore, the penetration seems to be insensitive to the current polarity, contrary to what is expected for a Hall-field induced penetration, rather than diffusion. In Ref. 22 we suggested a mechanism of Hall-induced penetration that relies on the formation of small-scale density nonuniformities in the plasma.

Another important issue is the fact that the magnetic-field penetration is accompanied by energy dissipation in the form of electron thermal energy.[13] Analysis of the electron energy distribution, in the context of the general energy balance in the plasma, will be presented in a future publication.[33]

A. Species separation

We have presented measurements of the dynamics of different charge-to-mass ratio ions under the propagation of the magnetic field. These measurements demonstrate that the heavy ions (heavier than protons in the present experiments) attain axial velocities that are significantly smaller than the magnetic-field velocity while protons are specularly reflected. As discussed in the preceding section, the electron-density drop at the magnetic-field front results from the proton reflection ahead of the current channel, while the density drop in the rear part of the current channel (after the reflection of the proton plasma) results from the carbon plasma dynamics. Thus, this work demonstrates that the species separation previously found in relatively short (<100 ns) current pulses[19,20] also occurs for longer pulses, higher electron densities, and smaller proton fractions.

The species separation and the reflection here observed can explain the flow of a dilute plasma downstream of the

prefilled-plasma region seen in previous experiments.[41,43] In those experiments, it was suggested that the downstream plasma flow was dominated by protons. It is worth mentioning that in such experiments the plasma flow downstream may affect the energy coupling to the load, due to current conduction by the plasma. It will be shown in Sec. IV E that similar to the observations in the shorter-time scale, the reflected ions obtain considerable momentum relative to their initial mass fraction, which reduces the momentum imparted on the heavy-ion plasma.

B. Effects of the time dependence of the magnetic field

Here we discuss implications of the rise in time of the current on the dynamics of the plasma. Interestingly, this time dependence results in proton velocities that are more than twice the magnetic piston velocity.

The 2D magnetic-field evolution[22] shows that the magnetic-field front can be approximated by a 1D structure, suggesting that the proton acceleration is mainly axial (in the $\vec{j}\times\vec{B}$ direction). As discussed in Sec. III D, however, the nonprotonic ions move significantly towards the electrodes, which will be further discussed in the following section.

Let us write a simplified expression that uses the magnetic-field distribution given by Eq. (1) and the measured time-dependent electron density shown in Fig. 9 to calculate the force acting in the axial direction on the nonprotonic ions. The single-particle ion momentum equation, neglecting collisions, is

$$m_i\frac{d\vec{v}_i}{dt}=ez_i\left(\vec{E}+\frac{\vec{v}_i\times\vec{B}}{c}\right). \tag{2}$$

Neglecting the electron inertia and resistivity in the electron momentum equation, assuming that the current is $\vec{J}=\vec{j}_e=-en_e\vec{v}_e$ (justified by the low values of the proton and nonprotonic ion velocities towards the electrodes), and employing Ampère's law (where the displacement current is neglected), we obtain the following expression for the electric field: $\vec{E}=-(\vec{v}_e\times\vec{B})/c=(\vec{j}_e/n_eec)\times\vec{B}=(\vec{\nabla}\times\vec{B})/4\pi\, n_e e\times\vec{B}=(\vec{\nabla}B^2)/8\pi\, n_e e$, which is the Hall electric field. Inserting this expression into Eq. (2), we assume that the current is mostly in the x direction and obtain through integration the following:

$$v_z(z_{in},t)=\frac{1}{8\pi}\frac{z_i}{m_i}\int_0^t\frac{1}{n_e[z(z_{in},t'),t']}\frac{\partial B[z(z_{in},t'),t']^2}{\partial z}dt', \tag{3}$$

where z_{in} is the initial ion location. This equation is integrated numerically with the assumption that for Li $z(z_{in},t)=z_{in}$. The results of the numerical integration are compared to the experimental velocities. For the integration we use a magnetic field given by Eq. (1) and an electron density that rises and drops linearly in time, down to a density of 1.5×10^{14} cm^{-3} (see the measurement in Fig. 9). Figure 10 shows the Li II velocity calculated using Eq. (3) for an initial position $z_{in}=3.5$ cm and the experimental average velocity at

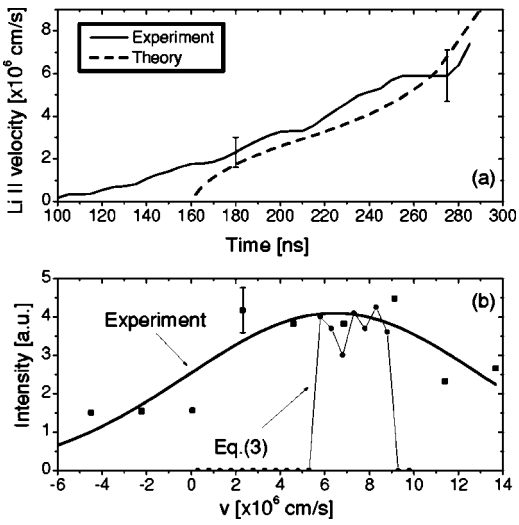

FIG. 10. (a) Comparison of the experimental Li II average velocity and the one calculated using Eq. (3) for $z=3.5$ cm. (b) Comparison of the experimental Li II velocity distribution and the one calculated using Eq. (3) for an initial homogenous ion distribution in the $z_{in}=2-5$ cm range at $t=280$ ns.

$z_{in}=3.5\pm1.5$ cm, demonstrating good agreement through most of the acceleration processes. The discrepancy for the times earlier than 160 ns results from the measurement spatial integration in the z direction (≈3 cm), which is not taken into account in using Eq. (3). The large experimental measurement uncertainty for $t>280$ ns does not allow for a useful comparison to the solution of Eq. (3).

In Fig. 10(b) the experimental Li II axial velocity distribution (previously shown in Fig. 4) is compared to the solution of Eq. (3), which is integrated over the initial lithium-ion positions ($z_{in}=2-5$ cm). It is evident that the observed distribution is much broader than the one predicted by Eq. (3).

The results of a similar comparison of the axially integrated C III velocity distribution at $t=300$ ns are shown in Fig. 11. The nonmonotonic distribution function of the C III ions found from the calculation is a result of the evolution in time of the magnetic field and of the plasma density that generates a group of fast ions at the back of the plasma as well as a group of slower ions at the front of the plasma. The

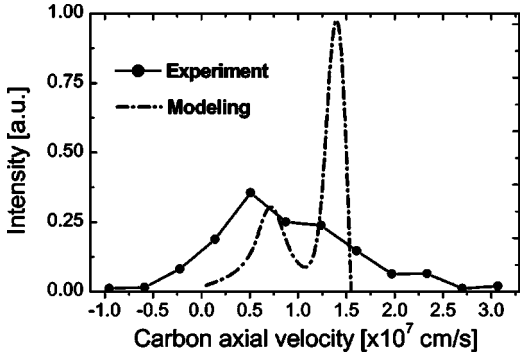

FIG. 11. The C III axial velocity distribution at $t=300$ ns obtained from the 2297 Å line. Also shown is the solution of Eq. (3), integrated over the entire axial plasma extent.

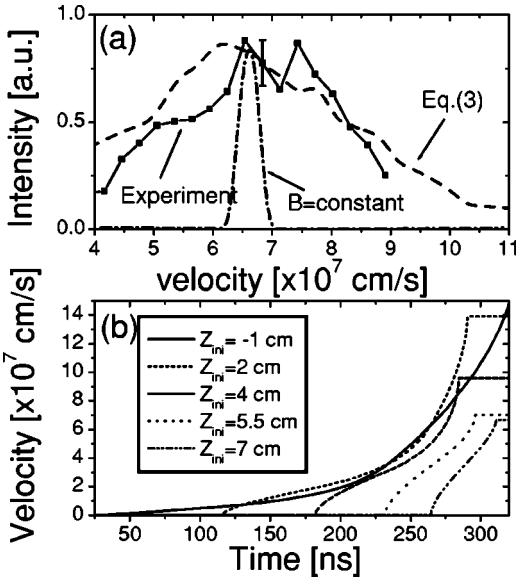

FIG. 12. (a) Comparison of the experimental proton-velocity distribution and the one calculated using Eq. (3) for $v_B=3.4\times10^7$ cm/s, averaged over $t=260-285$ ns. Also shown is the predicted proton-velocity distribution for a constant-amplitude magnetic field. (b) The calculated time-dependent proton velocity for five initial positions.

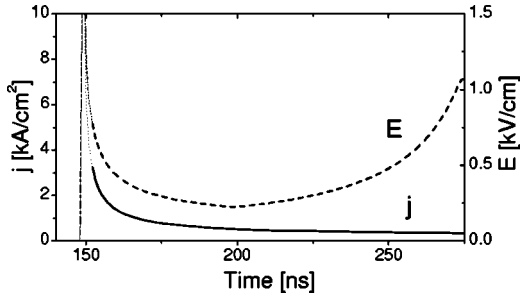

FIG. 13. The current density (solid line) and the accelerating Hall electric field (dashed) derived from the magnetic field given by Eq. (1) and the electron density time dependence employed in Eq. (3). The two lines are shown as dotted thin lines in the region where the accuracy of magnetic-field evolution of Eq. (1) could not be verified. The nonphysical infinity of the current density at $t=150$ ns, inherent in Eq. (1), is artificially truncated.

measured C III velocity distribution is found to be significantly broader than the solution of Eq. (3), similar to the results obtained above for Li II.

For predicting the proton dynamics the proton motion during the acceleration should be accounted for. We thus solve Eq. (3) together with $z=z_{in}+\int_0^t v(z_{in},t')dt'$ to obtain the final proton velocity as a function of z_{in}. We note that the proton dynamics cannot be obtained by solving a time-independent problem in the frame of the moving magnetic piston, as was previously done by Rosenbluth,[40] due to the rise in time of the magnetic field (in our experiment the magnetic-field changes significantly during the proton reflection).

In this calculation we find that a significant fraction of the protons attain a velocity that is larger than twice the magnetic-field velocity (while some of the protons that have not yet completed the reflection attain lower velocities). This observation may be understood by noting that in the frame of the moving piston the protons fall off a higher potential hill than the one they climb. Figure 12(a) shows the observed and the calculated axially integrated proton-velocity distributions. Both curves are time averaged over the time interval $t=260-285$ ns, required for accounting for the spatial integration over the hydrogen-dopant cloud. It is seen that the calculated distribution fits the experimental one rather well.

The importance of the magnetic-field time dependence can be further illustrated by a calculation for a constant-amplitude magnetic field shown by the dash-dot line in Fig. 12(a). We note, however, that the simple analysis here discussed does not account for various details that affect the proton-velocity distribution, such as the initial density distribution and the two-dimensional motion (where the latter may lead to a systematic loss of ions).

Figure 12(b) shows the acceleration of protons at different z_{in} for the same conditions as (a), demonstrating very different acceleration histories. Protons at $z_{in}=2$, 4, and 5.5 cm are reflected by the piston at $t\sim285$ ns while protons at $z_{in}=-1$ cm remain within the current channel up to $t=320$ ns. Also seen is the increase in the average acceleration as a function of z_{in}, resulting from the time dependence of the magnetic field during the axial propagation. The details of the ion dynamics are thus much affected by the current channel spatial distribution and the rise in time of the magnetic field.

It is interesting to note that the observed velocity distribution of the reflected ions (protons) can be reproduced with the solution of Eq. (3) while the measured velocity distribution of the ions in the plasma penetrated by the magnetic field (Li II and C III) is much broader than predicted according to Eq. (3). This difference suggests that our modeling of the ion acceleration is adequate in the front of the current channel in which the protons are reflected. In the back of the current channel the data suggest that, although the mean acceleration is consistent with the predictions of Eq. (3), as demonstrated by the Li II velocity in Fig. 10(a), there is another mechanism causing a significant broadening of the velocity distribution.

To further illustrate the difference between the reflected and nonprotonic-ion acceleration we plot in Fig. 13 the time-dependent current density j and the accelerating electric field E_{Hall}, obtained from the approximate time-dependent magnetic-field distribution given Eq. (1) for $z=3.7$ cm and the electron density time-dependence employed in Sec. IV B. The current density is sharply peaked in the magnetic-field front, followed by a extended tail that may result from the continuous generator-current rise in time. Available theoretical calculations based on the Hall model assume a magnetic field that is constant in time and hence cannot be employed to predict the expected current-density distribution behind the current front.

An important result that becomes clear from the data is that even a low current density in the back of the current channel ($t>170$ ns in Fig. 13) can result in significant ion acceleration due to the larger value of B there. Furthermore, the density drop that follows the proton reflection is accompanied by an increase in the accelerating electric field. It is

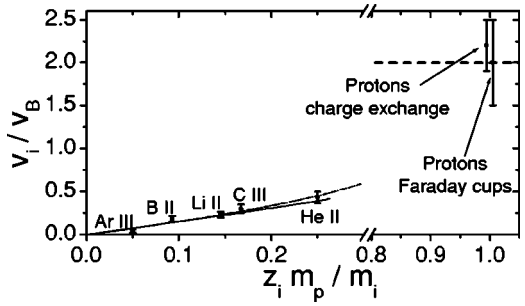

FIG. 14. Normalized peak ion axial velocities as a function of the ion charge-to-mass ratio at $x=1$, $y=0$, and $z=3.7$ cm. The dashed, solid, and dash-dot lines show the ion velocities expected for the protons and nonprotonic ions according to Eq. (3) and the velocity predicted for the nonprotonic ions that climb a constant-amplitude potential hill, respectively.

important to emphasize that due to the experimental uncertainties, our magnetic-field measurements do not allow for determining the exact structure of the magnetic-field front, allowing only for a qualitative interpretation of different acceleration regimes.

Noting that the proton reflection occurs within the front of the current channel ($t=150-250$ ns in Fig. 13) while the heavy-ion acceleration occurs continuously, we may conclude that the broad ion-velocity distribution originates in the back of the current channel, following the density drop. The previously suggested onset of the Rayleigh–Taylor instability[22] as a result of the proton acceleration could explain the broadening of the penetrated-ion velocity distributions (via fluctuations in the electron density and the accelerating field) while retaining the reflected ion-velocity distributions unaffected.

C. Scaling of the axial velocities with *Z*/*m*

In order to better understand the dynamics of different-mass ions it is instructive to plot the observed ion velocities as a function of the ion charge-to-mass ratio. Figure 14 shows the dependence of the measured axial ion velocities on the ion charge-to-mass ratio at the center of the plasma axial dimension ($z=3.7$ cm) for the time for which these velocities reach their peak values ($t\sim 270$ ns). The proton velocity is integrated along the line of sight and, thus, the velocity also reflects the velocity that the protons acquire at $z=3.7$ cm (at the axial center of the plasma). The velocities of He II and Ar III have been corrected to account for the ionization processes as discussed in Sec. III C. The dashed line indicates the velocity expected for ion reflection by a constant-amplitude potential hill,[40] which also agrees with the prediction of Eq. (3) for protons initially at $z=3.7$ cm.

The solid line represents the velocity of the nonprotonic ions in the plasma that is penetrated by the magnetic field ($v_i/v_B<1$) according to Eq. (3). Also shown in Fig. 14 is the prediction of a time-independent 1D model in which the ions climb over an electrostatic potential $B_{eff}^2/8\pi n_e$, where B_{eff} is an effective time-averaged magnetic-field amplitude. The final normalized ion velocities are then given by $v_i/v_{mf}=1-\sqrt{1-[z_i/(m_i/m_p)/(v_{Ap}^2/v_{mf}^2)]}$, where v_{Ap} is the Alfvén velocity assuming the plasma only consists of protons. We find that in order to fit the measured velocities $B_{eff}=5.1$ kG, reflecting an average value for the rising-in-time magnetic field. One can see that both models explain the heavy-ion velocities to within the experimental uncertainties.

D. Ion motion towards the electrodes

The understanding of the ion dynamics also requires knowledge of the ion velocities in the *A*-*K* gap (x) direction. In our experiment, these are inferred from the time dependence of the electron density.

Since most of the protons in the plasma are found, due to their reflection, at 4–8 cm downstream of the plasma (and the *A*-*K* gap is 2.5 cm wide), it can be inferred that their velocities (v_x) in the x direction are $<v_z/4$, where v_z is the z-direction velocity. Such values for v_x are comparable to the initial v_x of the protons ($\approx 10^7$ cm/s). It thus appears that the protons nearly undergo 1D specular reflection.

For the carbon ions, however, their v_x appears to be comparable to $v_z(\approx 10^7$ cm/s). This is inferred from the electron-density drop (see Fig. 9), which is significantly larger than expected from the proton reflection, and cannot be explained by the slow motion of the carbon plasma and the larger plasma dimension in the axial direction. Since the initial v_x of the carbon ions is $\approx 5\times 10^6$ cm/s, the higher v_x during the current conduction can only be explained by x components of the $\vec{j}\times\vec{B}$ forces in the field-penetrated plasma. In the present experiment, however, this cannot be compared to the 2D magnetic-field structure in the plasma[22] because of the large uncertainties. Note that the presence of $\vec{j}\times\vec{B}$ components in the x direction may also be observed on a small spatial scale (<1 mm) consistent with our suggestion on possible small-scale variations in the plasma density and the magnetic-field,[22] however, such variations are not observable in the present 1 cm spatial-resolution measurements.

It is worth mentioning a recent suggestion[44] that ions may move in the x direction even in the absence of x components of the $\vec{j}\times\vec{B}$ forces. It was there shown that in a multi-ion-species plasma, ions of different masses may gain significant (and opposite) momenta in the direction of the current, while the net ion acceleration is only in the $\vec{j}\times\vec{B}$ direction (as expected).

E. Momentum balance

We now analyze the momentum gained by the plasma due to the interaction with the magnetic field. The total momentum per unit area imparted to the plasma by the $\vec{j}\times\vec{B}$ forces is given by

$$P(t)=\frac{1}{8\pi}\int_0^t B(z=z_0,t')^2 dt', \tag{4}$$

where Eq. (1) is used for $B(z=z_0,t)$. Integration of Eq. (4) yields $P(t)=B_0^2t^3/24\pi\tau^2$, which gives $P=0.40$ g/(cm s) at $t=\tau=300$ ns [note that P is $3\times$ smaller than the momentum imparted by a constant (B_0) magnetic field]. Assuming that the plasma density and composition are uniform in space and

that the plasma is composed of protons and triply charged carbon ions, the plasma momentum per unit area can be approximated by $P_{plasma}(t)=(n_p m_p\langle v_p\rangle + n_c m_c\langle v_{C\ IV}\rangle)\ \Delta z$, where n_p and n_c are the densities and m_p and m_c are the masses of the protons and of the carbon ions, respectively. $\langle v_p\rangle$and $\langle v_{C\ IV}\rangle$ are the respective time-dependent velocities averaged over z up to $\Delta z \approx v_B t$, which is the magnetic-field axial-propagation distance. $\langle v_{C\ IV}\rangle$ is estimated from a linear scaling with the ion charge of the experimental C III velocity distribution shown in Fig. 11, giving $\langle v_{C\ IV}\rangle = 1.1 \times 10^7$ cm/s. For the protons we use Fig. 7 and assume that the mean velocity presented there is also valid at $t=300$ ns, yielding $\langle v_p\rangle = 6.8\times 10^7$ cm/s.

Inserting these velocities and the initial ion densities leads to the conclusion that the protons and the nonprotonic ions attain equal fractions of the imparted momentum. Hence, the protons whose mass fraction in the initial plasma is only 13% attain ≈50% of the imparted momentum. The total plasma momentum at $t=300$ ns is $P_{\text{plasma}} = 0.48$ g/(cm s), which is ≈20% larger than the imparted momentum, calculated from Eq. (4). The discrepancy probably results from the assumption that the magnetic-field propagation velocity v_B is constant throughout the pulse (indeed, based on the magnetic-field measurements, the true Δ_z is ≈20% smaller than used in the estimates above, due to the lower magnetic-field velocity in the first 100 ns of the pulse).

Incidentally, taking a constant magnetic field ($B=6$ kG), which is smaller than the maximal value of B, and inserting this into the simplified model for the case of a constant magnetic field[20] yield a similar partitioning of the momentum.

V. SUMMARY

Spatially and temporally resolved measurements of the magnetic field, electron density, and ion velocities in a multi-ion-species plasma interacting with a propagating magnetic field are presented. The data obtained demonstrate self-consistencies between the ion velocities, the electric field determined from the magnetic field and the electron density, and the momentum imparted to the plasma due to the magnetic-field pressure. We find that similarly to the results reported for a shorter time-scale experiment,[19,20] species separation occurs in which the light-ion plasma is pushed ahead of the magnetic piston, while the heavier-ion plasma is penetrated by the magnetic field. The observation that some of the reflected protons attain velocities larger than twice the magnetic-field velocity (the velocity attained in a specular reflection by a constant-amplitude magnetic field[40]) is explained by the time dependence of the magnetic field.

In this paper we discussed the different aspects of the ion dynamics, including the proton reflection and the resulting ion-species separation. We emphasize that, considering all data obtained, the mechanism of magnetic-field penetration into the plasma in the present experiment, with the simultaneous light-ion reflection, that is, pushed by the magnetic-field pressure, is not entirely clear. It was suggested that the proton reflection may induce density fluctuations that allow for polarity-independent field penetration due to the Hall field. A model that correctly predicts the magnetic-field propagation velocity and the independence of the velocity on the current flow direction is still required.

Our results show that significant acceleration of the nonprotonic ions occurs in the region behind the magnetic-field front, in which the current density is low. Also, the ion-velocity distribution of the nonprotonic ions (in the plasma penetrated by the magnetic field) in the propagation direction of the magnetic field is found to be much broader than expected. The mechanism responsible for the relatively high velocities of these ions in the direction normal to the field propagation direction remains unclear. One possible mechanism that may explain both observations is the previously suggested onset of small-scale density fluctuations,[22] perhaps as a result of the Rayleigh–Taylor instability.

These findings have important implications to a variety of pulsed-power systems and to high-power transmission lines. For example, these observations may aid in the optimization of plasma-opening-switch performance and in improving the coupling of the switched power to various loads.[45] The comparisons of the results obtained here and in previous studies on similar current experiments with those obtained in other higher-current experiments may provide an insight into the factors that limit the efficiency of plasma switches.[46] The importance of the initial plasma composition has become evident due to the ion species separation and due to its affect on the momentum partitioning between the different-ion species, and is presumably highly important for optimizing the switch operation. Previous investigations of the POS operation, in which a novel method was implemented for producing plasmas of controllable purity, have been reported on.[47,48] Currently, better control of the plasma composition is pursued[49,50] in the present configuration in order to study the dependence of the phenomena observed here on this parameter. Also, improved doping capabilities should allow for further studying the mechanisms responsible for the ion velocities in the normal directions.

It should also be noted that such detailed results as the ones described here may be employed for examining various plasma-simulation codes required for the design of electrical discharges, plasma switches, high-power transmission lines, and analysis of space-physics data.

ACKNOWLEDGMENTS

The authors wish to thank Dr. Ya. E. Krasik for his assistance with the Faraday-cup measurements and in the design of the experiment. We are grateful to A. Fisher, A. Weingarten, and R. Doron for their valuable suggestions. We are in indebted to P. Meiri for his skilled technical assistance.

This work was supported by the German-Israeli Project Cooperation Foundation (DIP), the Minerva Foundation, the United States–Israel Binational Science Foundation, the Israel science foundation, and by Sandia National Laboratories.

[1] R. J. Commisso and H. R. Griem, Phys. Fluids **20**, 44 (1977).
[2] T. A. Mehlhorn, IEEE Trans. Plasma Sci. **25**, 1336 (1997), and references therein.
[3] See, for example, *"Special Issue on Plasma Opening Switches"*, IEEE

Trans. Plasma Sci. **PS-15**, (1987), and references therein.
[4]W. Peter, A. Ron, and N. Rostoker, Phys. Fluids **26**, 2276 (1983).
[5]S. B. Mende, G. R. Swenson, S. P. Geller, J. H. Doolittle, G. Haerendel, A. Valenzuela, and O. H. Bauer, J. Geophys. Res. **94**, 17063 (1989).
[6]K. J. H. Phillips, Plasma Phys. Controlled Fusion **42**, 113 (2000).
[7]C. Litwin, R. Rosner, and D. Q. Lamb, Mon. Not. R. Astron. Soc. **310**, 324 (1999).
[8]A. S. Kingsep, Yu. V. Mohkov, and K. V. Chukbar, Sov. J. Plasma Phys. **10**, 495 (1984).
[9]A. V. Gordeev, A. S. Kingsep, and L. I. Rudakov, Phys. Rep. **243**, 215 (1994).
[10]A. Fruchtman, Phys. Fluids B **3**, 1908 (1991).
[11]R. Shpitalnik, A. Weingarten, K. Gomberoff, Ya. Krasik, and Y. Maron, Phys. Plasmas **5**, 792 (1998).
[12]M. Sarfaty, Y. Maron, Ya. E. Krasi, A. Weingarten, R. Arad, R. Shpitalnik, A. Fruchtman, and S. Alexiou, Phys. Plasmas **2**, 2122 (1995).
[13]A. Fruchtman, Phys. Rev. A **45**, 3938 (1992); A. Fruchtman, A. A. Ivanov, and A. S. Kingsep, Phys. Plasmas **5**, 1133 (1998).
[14]A. Fruchtman, J. M. Grossman, S. B. Swanekamp, and P. F. Ottinger, IEEE Trans. Plasma Sci. **27**, 1464 (1999).
[15]R. J. Commisso and H. J. Kunze. Phys. Fluids **18**, 392 (1975).
[16]J. Bailey, Y. Ettinger, A. Fisher, and N. Rostoker, Appl. Phys. Lett. **40**, 460 (1982); G. Barak and N. Rostoker, *ibid.* **41**, 918 (1982).
[17]C. W. Mendel, Jr., Phys. Rev. A **27**, 3258 (1983).
[18]L. I. Rudakov, Phys. Plasmas **2**, 2940 (1995).
[19]A. Weingarten, C. Grabowski, A. Fruchtman, and Y. Maron, *Proceedings of the XIIth International Conference on High-Power Particle Beams, Haifa, Israel, 1998*, edited by M. Markovits and J. Shiloh (IEEE, Piscataway, NJ, 1998), Vol. 1, p. 346.
[20]A. Weingarten, R. Arad, A. Fruchtman, and Y. Maron, Phys. Rev. Lett. **87**, 115004 (2001).
[21]R. Arad, Ph.D. thesis, Weizmann Institute of Science Rehovot, Israel, 2002; K. Tsigutkin, R. Arad, A. Fisher, and Y. Maron, *Proceedings of the 13th International Conference on High-Power Particle Beams, Nagaoka, 2000*, edited by K. Yatsui and W. Jiang (Nagaoka University of Technology, Nagaoka, 2001), p. 111.
[22]R. Arad, K. Tsigutkin, A. Fruchtma, J. D. Huba, and Y. Maron, Phys. Plasmas **10**, 112 (2003).
[23]C. W. Mendel, Jr. and S. A. Goldstein, J. Appl. Phys. **48**, 1004 (1977).
[24]H. J. Kunze, in *Plasma Diagnostics*, edited by W. Lochte-Holtgreven (North-Holland, Amsterdam, 1968).
[25]L. Perelmutter, G. Davara, and Y. Maron, Phys. Rev. E **50**, 3984 (1994); K. Tsigutkin, E. Stambulchik, R. Doron, D. Osin, V. Bernshtam, Y. Ralchenko, and Y. Maron, *Proceedings of the 14th IEEE International Pulsed Power Conference, Dallas, TX, 2003* (IEEE, Piscataway, NJ, 2003), Vol. 2, p.785.
[26]B. V. Weber and D. D. Hinshelwood, Rev. Sci. Instrum. **63**, 5199 (1992); B. V. Weber and S. F. Fulghum, *ibid.* **68**, 1227 (1997).
[27]A. Chuvatin and B. Etlicher, Phys. Rev. Lett. **74**, 2965 (1995).
[28]D. D. Hinshelwood, B. V. Weber, J. M. Grossmann, and R. J. Commisso, Phys. Rev. Lett. **68**, 3567 (1992).
[29]G. G. Spanjers, E. J. Yadlowsky, R. C. Hazelton, and J. J. Moschella, J. Appl. Phys. **77**, 3657 (1995).
[30]D. D. Hinshelwood, R. J. Commisso, P. J. Goodrich, J. M. Grossimann, J. C. Kellogg, P. F. Ottinger, and B. V. Weber, *Proceedings of the 8th International Conference on High-Power Particle Beams, Novosibirsk, 1990*, edited by B. N. Breizman and B. A. Knyazev (World Scientific, Singapore, 1990), p. 1035.
[31]R. Arad, L. Ding, and Y. Maron, Rev. Sci. Instrum. **69**, 1529 (1998).
[32]R. Arad, K. Tsigutkin, Yu. V. Ralchenko, and Y. Maron, Phys. Plasmas **7**, 3797 (2000).
[33]R. Arad, Yu. V. Ralchenko, A. Fruchtman, and Y. Maron, Phys. Rev. E. (submitted).
[34]C. W. Mendel, Jr. (private communication).
[35]D. G. Colombant and B. V. Weber, IEEE Trans. Plasma Sci. **PS-15**, 741 (1987); B. V. Weber, R. J. Commisso, G. Cooperstein *et al.*, *ibid.* **PS-15**, 635 (1987); R. W. Stinnet, *ibid.* **PS-15**, 557 (1987); T. J. Renk, J. Appl. Phys. **65**, 2652 (1989).
[36]Yu. V. Ralchenko and Y. Maron, J. Quant. Spectrosc. Radiat. Transf. **71**, 609 (2001).
[37]R. Arad, K. Tsigutkin, A. Fruchtman, and Y. Maron, *Proceedings of the XIIth International Conference on High-Power Particle Beams Haifa, Israel, 1998*, edited by M. Markovits and J. Shiloh (IEEE, Piscataway, NJ, 1998), Vol. 1, p. 253.
[38]V. A. Belyaev, B. G. Brezhnev, and E. M. Erastov, Sov. Phys. JETP **25**, 777 (1967); J. H. Newman, J. D. Cogan, D. L. Ziegler, D. E. Nitz, R. D. Runder, K. A. Smith, and P. F. Stebbigs, Phys. Rev. A **25**, 2976 (1982).
[39]P. Hvelplund and A. Andersen, Phys. Scr. **26**, 375 (1982); Yu. S. Gordeev and M. N. Panov, Sov. Phys. Tech. Phys. **9**, 656 (1964); F. Schwirzke, Z. Phys. **157**, 510 (1960).
[40]M. N. Rosenbluth, in *Progress in Nuclear Energy, Series XI: Plasma Physics and Thermonuclear Research*, edited by C. L. Longmire, J. T. Tuck, and W. B. Thompson (Pergamon, London, 1963), Vol. 2, pp. 217–277.
[41]Ya. E. Krasik and A. Weingarten, IEEE Trans. Plasma Sci. **26**, 208 (1998).
[42]A. Weingarten, V. A. Bernshtam, A. Fruchtman, C. Grabowski, Ya. E. Krasik, and Y. Maron, IEEE Trans. Plasma Sci. **27**, 1596 (1999).
[43]B. V. Weber, D. D. Hinshelwood, and R. J. Commisso, IEEE Trans. Plasma Sci. **25**, 189 (1997).
[44]N. Chakrabarti, A. Fruchtman, R. Arad, and Y. Maron, Phys. Lett. A **297**, 92 (2002).
[45]J. R. Thompson, P. L. Coleman, R. J. Crumley, P. J. Goodrich, J. R. Goyer, J. E. Rauch, Y. Maron, and J. J. Moschella, *Proceedings of the 12th IEEE Pulsed-Power Conference Monterey, Ca, 1999*, edited by C. Stallings and H. Kirbie (IEEE, Piscataway, NJ, 1999), p. 210.
[46]R. Arad, A. Weingarten, K. Tsigutkin *et al.*, *Proceedings of the International Power-Modulator Conference & High-Voltage Workshop Hollywood, CA, 2002*, edited by M. A. Gundersen (IEEE, Piscataway, NJ, 2002), p. 17.
[47]J. J. Moschella, R. C. Hazelton, C. Vidoli *et al.*, *Proceedings 12th International Conference High-Power Particle Beams, Haifa, Israel, 1998*, edited by M. Markovits and J. Shiloh (IEEE, Piscataway, NJ, 1998), Vol. I, p. 306; J. J. Moschella, R. C. Hazelton, C. Vidoli, and E. J. Yadlowsky, IEEE Trans. Plasma Sci. **28**, 2247 (2000).
[48]P. S. Ananjin, V. P. Karpov, Ya. E. Krasik, I. V. Litsitzin, A. V. Petrov, and V. G. Tolmacheva, IEEE Trans. Plasma Sci. **20**, 537 (1992).
[49]D. Osin, R. Arad, K. Tsigutkin, V. Bernshtam, A. Starobinets, Y. Maron, and A. Fisher, IEEE Trans. Plasma Sci. (submitted).
[50]R. Doron, R. Arad, K. Tsigutkin *et al.*, Phys. Plasmas **11**, 2411 (2004).